Journal of Advanced Ceramics
2022, **11**(6): 882–892
https://doi.org/10.1007/s40145-022-0582-6
ISSN 2226-4108
CN 10-1154/TQ

Research Article

Self-ball milling strategy to construct high-entropy oxide coated $LiNi_{0.8}Co_{0.1}Mn_{0.1}O_2$ with enhanced electrochemical performance

Kai YUAN[a], Tianzhe TU[b], Chao SHEN[a,c,*], Lin ZHOU[b], Jixuan LIU[b,*], Jing LI[d], Keyu XIE[a,c], Guojun ZHANG[b]

[a]*State Key Laboratory of Solidification Processing*, *Center for Nano Energy Materials*, *School of Materials Science and Engineering*, *Northwestern Polytechnical University*, *Xi'an 710072*, *China*
[b]*State Key Laboratory for Modification of Chemical Fibers and Polymer Materials*, *Institute of Functional Materials*, *College of Materials Science and Engineering*, *Donghua University*, *Shanghai 201620*, *China*
[c]*Research & Development Institute of Northwestern Polytechnical University in Shenzhen*, *Northwestern Polytechnical University*, *Shenzhen 518057*, *China*
[d]*State Key Laboratory of Environment-friendly Energy Materials*, *School of Materials Science and Engineering*, *Southwest University of Science and Technology*, *Mianyang 621010*, *China*

Received: November 25, 2021; Revised: January 26, 2022; Accepted: February 19, 2022

Abstract: High-entropy oxides (HEOs) are a new class of emerging materials with fascinating properties (such as structural stability, tensile strength, and corrosion resistance). High-entropy oxide coated Ni-rich cathode materials have great potential to improve the electrochemical performance. Here, we present a facile self-ball milling method to obtain $(La_{0.2}Nd_{0.2}Sm_{0.2}Eu_{0.2}Gd_{0.2})_2Zr_2O_7$ (HEO) coated $LiNi_{0.8}Co_{0.1}Mn_{0.1}O_2$ (NCM811). The HEO coating endows NCM811 with a stable surface, reduces the contact with the external environment (air and electrolyte), and inhibits side reactions between cathode and electrolyte. These favorable effects, especially when the coating amount is 5 wt%, result in a significant reduction of the battery polarization and an increase in the capacity retention from 57.3% (NCM811) to 74.2% (5HEO-NCM811) after 300 cycles at 1 C (1 C = 200 $mA{\cdot}h{\cdot}g^{-1}$). Moreover, the morphology and spectroscopy analysis after the cycles confirmed the inhibitory effect of the HEO coating on electrolyte decomposition, which is important for the cycle life. Surprisingly, HEO coating reduces the viscosity of slurry by 37%–38% and significantly improves the flowability of the slurry with high solid content. This strategy confirms the feasibility of HEO-modified Ni-rich cathode materials and provides a new idea for the design of high-performance cathode materials for Li-ion batteries.

Keywords: high-entropy oxides (HEOs); Li-ion battery (LIB); Ni-rich cathode; coating modification

* Corresponding authors.
E-mail: C. Shen, shenchao@nwpu.edu.cn;
J. Liu, jxliu@dhu.edu.cn

1 Introduction

The boom in renewable energy, various portable electronic devices, and electric vehicles have driven advances in advanced battery technology [1]. Li-ion battery (LIB) is an undeniable pioneer with increasing energy density at a manageable cost [2]. Nowadays, Ni-rich cathode materials $LiNi_xM_{1-x}O_2$ ($x \geqslant 0.6$, M = Co, Al, Mn, Ti, etc.) are considered as the up-and-coming ones for LIBs to meet the needs of the high density energy storage demands [3,4]. However, some intractable issues hinder the large-scale commercial application of Ni-rich cathode materials, such as serious side reactions between cathode and electrolyte resulting in the decomposition of electrolyte, the formation of a thicker cathode electrolyte interphase (CEI), and the corrosion and pulverization of the active materials. These issues are responsible for the degradation of electrochemical performance [5,6]. Therefore, it is particularly important to overcome the above problems to break through the restrictions of the commercial application of Ni-rich materials.

Among various modification methods, surface coating is one of the most effective strategies [7]. Until now, various materials have been used as the surface coating materials for Ni-rich cathodes, such as metal oxides, phosphates, organic polymers, and carbon materials [4,8–13]. According to previous works, the ideal surface coating should meet the following conditions: (1) The coating materials do not change the crystal structure of the cathode material, (2) the coating layer is thin enough and well dispersed so as not to reduce the conductivity, (3) the coating layer can inhibit the degradation of cathode material, and (4) the coating process does not increase the cost of the material too much.

High-entropy (HE) materials, as an emerging concept in recent years, combine with more than five elements (the concentration of each element is between 5 and 35 at%) to create new single-phase materials with a configuration entropy (S_{config}) $\geqslant 1.5R$ [14–17]. This concept has been applied in various fields. In particular, with the application in energy storage first reported in 2018, high-entropy oxides and their derivatives have attracted much attention [18–20]. At present, it has been used as LIB cathode materials [21,22], anode materials [23], and sodium-ion battery cathode materials [24]. It is easy to find from previous studies that high-entropy oxides are ideal coating materials for the electrochemical active material because of its advantages (such as structural stability due to high entropy) [25]. Unfortunately, to our best, there is no report about high-entropy oxides modified battery active materials, especially high-entropy oxides modified Ni-rich cathode materials.

Herein, a simple and inexpensive strategy for high-entropy oxide coated NCM811 has been proposed for the first time. Through mixing NCM811 microspheres and nano $(La_{0.2}Nd_{0.2}Sm_{0.2}Eu_{0.2}Gd_{0.2})_2Zr_2O_7$ (HEO) particles, self-ball milling, and low-temperature heat treatment, the roughly HEO coating NCM811 was achieved. As shown in Fig. 1, the HEO coating can reduce the contact of NCM811 with the surrounding environment (air and electrolyte) and inhibit the side reactions on the electrode–electrolyte interface. Most intuitively, the HEO coating significantly reduces the viscosity and increases the flowability of slurry at a high solid content. In comparison with the uncoated counterpart, the sample with 5 wt% HEO coated (5HEO-NCM811) delivers enhanced cycling stability (74.2% capacity retention vs. 57.3% of NCM811 after 300 cycles at 1 C (1 C = 200 $mA \cdot h \cdot g^{-1}$)). In addition, the slurry of 5HEO-NCM811 has a lower viscosity and better processability at the same solid content, thanks to lower surface lithium impurities. Owing to the simplicity, efficiency, and low cost of the method, this strategy can be used for coating modification of HE substances in other electrode materials.

2 Experimental

2.1 Synthesis of $La_{0.2}Nd_{0.2}Sm_{0.2}Eu_{0.2}Gd_{0.2})_2Zr_2O_7$ and HEO coated NCM

The $(La_{0.2}Nd_{0.2}Sm_{0.2}Eu_{0.2}Gd_{0.2})_2Zr_2O_7$ (HEO) powder was synthesized at 1300 ℃ in the air by solid-state

Fig. 1 Schematic illustration of coating process of NCM811 with HEO.

reaction method using La_2O_3, Nd_2O_3, Sm_2O_3, Eu_2O_3, Gd_2O_3, and ZrO_2 as raw materials. Detailed information was reported in our previous work [26]. The HEO coated NCM811 was synthesized by a self-ball milling method. This novel method can be concluded as using the NCM811 microparticles as the mill balls combined with low-temperature heat treatment. To acquire the composites, firstly, the prepared HEO was mixed with NCM811 at different ratios. Then the mixtures were ball-milled. Finally, the mixtures were sintered at 300 ℃ in air for 1 h. After cooling to room temperature, the HEO coated NCM811 composites were finally obtained. For comparison, the different surface coating ratios of 1, 3, 5, and 10 wt% were tried (denoted as 1HEO-NCM811, 3HEO-NCM811, 5HEO-NCM811, and 10HEO-NCM811, respectively).

2. 2 Material characterization

The phases of HEO, NCM811, and HEO coated NCM811 were analyzed by the X-ray diffractometer (X'Pert PRO MPD diffractometer, Cu Kα radiation) in the 2θ range of 10°–80°. The scanning electron microscope (SEM, FEI Nano SEM 450) was utilized to evaluate the surface morphology of all the samples. The X-ray photoelectron spectroscope (XPS, Thermo SCIENTIFIC ESCALAB 250Xi) was employed to investigate the chemical compositions of these samples. The rheometer (HAAKE, MARS III) was used to realize the rheological tests of the slurry. The tests were conducted immediately after the completion of the slurry mixing process, where a steady-state flow test and an oscillation test were performed to evaluate the viscosity and the stability of the slurry, respectively. The flow curves were carried out for shear rates ranging from 1 to 200 and the oscillation tests for τ ranging from 10^{-2} to 10^{3}. Each test consisted of 50 steps and was performed at 25 ℃. The detailed test parameters were described in the previous studies [4,27].

2. 3 Assessment of electrochemical performances

To evaluate the electrochemical performances of these materials, CR2032 coin half-cells were assembled in a glovebox filled with argon. 1.0 M $LiPF_6$ in a mixture of ethylene carbonate (EC)/dimethyl carbonate (DEC)/ ethyl methyl carbonate (EMC) (volume ratio = 1:1:1) was used as the electrolyte. The amount of electrolyte used in the cell is around 80 μL (electrolyte volume: cathode material weight = 1 L:25 g). The separator and anode were a porous polypropylene membrane (Celgard2500) and a lithium metal disc with a diameter of 15 mm, respectively. The cathode electrodes were fabricated by mixing the active material, poly(vinyl difluoride) (PVDF), and acetylene black (AB) in a weight ratio of 8:1:1 with the solvent of N-methyl-2-pyrrolidone (NMP). Then the homogenized slurries were coated on Al foil and dried at 100 ℃ for 8 h under vacuum. The prepared cathode electrodes were cut to disks with a diameter of 12 mm, and the mass loading of the electrode is ~2 $mg \cdot cm^{-2}$. The assembled half-cell was cycled at a galvanostatic charge/discharge in the LAND CT2001A battery test instrument with a specified current density between 2.8 and 4.3 V (vs. Li^+/Li). The electrochemical impedance spectroscopy (EIS) was performed with a frequency range of 10^{-2}–10^{5} Hz after 300 cycles. Cyclic voltammetry (CV) was carried out on a Solartron Electrochemical Workstation (UK 1260+1287).

3 Results and discussion

The morphologies of the HEO nanoparticles, NCM811, and HEO coated NCM811 were observed by SEM as shown in Fig. S1 in the Electronic Supplementary Material (ESM) and Fig. 2. The prepared HEO is a flake powder with a size of ~100 nm (Figs. S1(a) and S1(b) in the ESM). Figures S1(c)–S1(h) in the ESM show that 6 elements (Zr, Nd, Eu, Sm, La, and Gd) are relatively uniformly distributed in the HEO. The high-resolution SEM image shows that the contour of the NCM811 primary particles is clearly visible and smooth. However, HEO nano-flakes appeared on the surface of the coated NCM811. When the coating amount is 1 wt% (Figs. 2(c) and 2(d)), the nano-flakes mainly appear on the boundary of the primary particles. Increasing the amount of HEO (Figs. 2(e)–2(i)), the nanosheets become more and gradually cover the surface of NCM811 so that the original boundary between the primary particles cannot be distinguished. From the energy dispersive spectroscopy (EDS) mapping results, the Ni, Co, and Mn belonging to NCM811 are uniformly distributed. Elements (Zr, Nd, Eu, Sm, La, and Gd) belonging to HEO are also observed and are evenly distributed on the surface of HEO-NCM811, but the distribution is sparse compared to the elements of Ni, Co, and Mn. This is due to the low content of HEO in the composite.

Figures 3(a) and 3(b) show the X-ray diffraction (XRD) patterns of HEO, NCM811, and 5HEO-NCM811. The prepared HEO is single-phase and has a pyrochlore structure [26,28,29]. NCM811 and 5HEO-NCM811 conform to the hexagonal α-$NaFeO_2$ crystal structure and belong to the $R\bar{3}m$ space group [30]. The clearly splitting (006)/(102) and (108)/(110) peaks reveal that these two materials have a well-ordered layered structure [31,32]. In the XRD pattern of 5HEO-NCM811, the characteristic peak of HEO at 29° can be clearly found, but not observed in that of NCM811. This indicates that HEO has been successfully coated on the surface of NCM811, which is consistent with the results observed by the SEM.

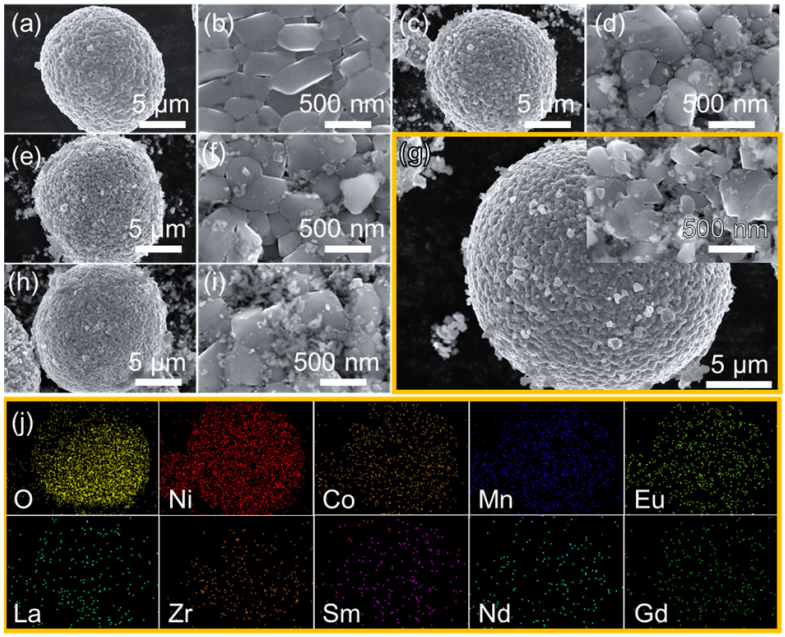

Fig. 2 SEM images of (a, b) NCM811, (c, d) 1HEO-NCM811, (e, f) 3HEO-NCM811, (g) 5HEO-NCM811, and (h, i) 10HEO-NCM811. (j) Elemental mappings of O, Ni, Co, Mn, Eu, La, Zr, Sm, Nd, and Gd of 5HEO-NCM811.

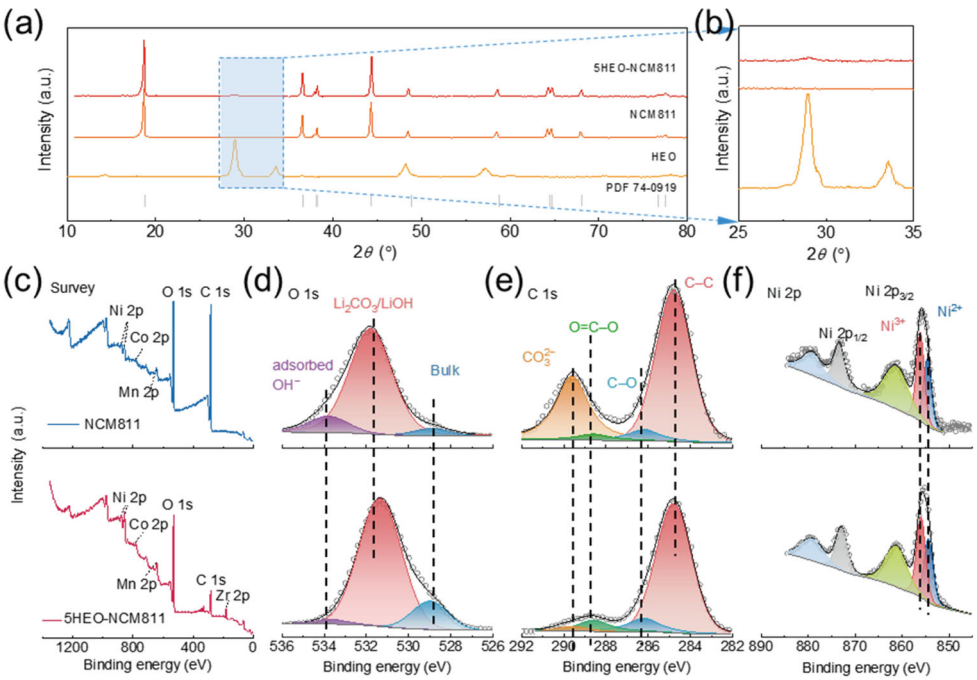

Fig. 3 (a) XRD patterns of NCM811, 5HEO-NCM811, and HEO from 10° to 80° and (b) enlarged XRD patterns in (a) from 25° to 35°. XPS spectra of (c) survey, (d) O 1s, (e) C 1s, and (f) Ni 2p of NCM811 (top) and 5HEO-NCM811 (bottom).

To study the effect of HEO coating on the surface chemistry of NCM811, XPS analysis was performed to determine the surface element types, chemical environment, and valence state. Both of the survey spectra of NCM811 (top) and 5HEO-NCM811 (bottom), as shown in Fig. 3(c), have obvious peaks of Ni 2p, Co 2p, Mn 2p, O 1s, and C 1s. However, the Zr 3d peak only appeared in the survey spectrum of HEO-NCM811, which once again proved that HEO was successfully coated on the surface of NCM811. In addition, the relative peak intensity of C 1s in the survey spectrum of NCM811 is significantly higher than that of 5HEO-NCM811. The possible reason is that the HEO coating reduces the contact of NCM811 with carbonaceous substances (such as CO_2) in the air [33]. High-resolution XPS spectra of O 1s (Fig. 3(d)) and C 1s (Fig. 3(e)) were used to further study the effect of HEO coating layer on the adsorbate on the surface of NCM811. The O 1s peaks of bulk materials, Li_2CO_3/LiOH, and adsorbed OH^- are located at 529.0, 531.8, and 533.8 eV, respectively [34]. It is worth noting that the percentages of adsorbed OH^- and Li_2CO_3/LiOH on the surface of NCM811 are 11.8% and 83.4%, respectively, while those on the surface of 5HEO-NCM811 are 3.2% and 81.7%, respectively (Table 1). The collected C 1s spectra contained species mainly derived from the adventitious carbon (284.8 eV), C–O (286.2 eV), O–C=O (288.6 eV), and carbonate (289.6 eV) [35]. The contents of CO_3^{2-} on the surface of NCM811 and 5HEO-NCM811 are 29.9% and 2.5%, respectively. For NCM811, even if it is stored in vacuum, and the contact with air is minimized during operation, carbonates will be formed on the surface. In contrast, under the same storage conditions and operation processes, the amount of carbonate formed on the surface of 5HEO-NCM811 is significantly reduced. This proves in another way that the HEO coating can inhibit the reaction of NCM811 with the air.

Table 1 Contents of each parts in the O 1s, C 1s, and Ni 2p XPS spectra in Figs. 3(d)–3(f) (Unit: %)

	O 1s			C 1s				Ni 2p	
	Adsorbed OH^-	Li_2CO_3/LiOH	Bulk	C–O	O=C–O	CO_3^{2-}		Ni^{3+}	Ni^{2+}
NCM811	11.8	83.4	4.8	5.9	3.1	29.9		56.8	43.2
5HEO-NCM811	3.2	81.7	15.1	10.5	8.0	2.5		54.1	45.9

The valence states of Ni in Ni-rich materials have an important influence on the electrochemical performance [36]. In particular, Ni^{2+} will increase cation mixing, aggravate the deterioration of the material structure, and ultimately reduce the capacity and accelerate the capacity decay. It has been previously reported that some ion dopings (such as W^{5+}) or some coatings (such as $LiNbO_3$) will increase the content of Ni^{2+} [37–39]. The high-resolution XPS spectra of Ni 2p in NCM811 and 5HEO-NCM811 are shown in Fig. 3(f). The peaks of Ni^{3+} and Ni^{2+} are located at ~856.5 and ~855 eV, respectively. The Ni^{2+} contents of the two materials are close (56.8% for NCM811 and 54.1% for 5HEO-NCM811) (Table 1). This means that the HEO coating of this strategy does not affect the oxidation valence of Ni. The high-resolution XPS spectra of Sm 3d, Gd 4d, Eu 4d, and Zr 3d of the two samples are shown in Fig. S2 in the ESM. In comparison, the characteristic peaks of Sm 3d, Gd 4d, Eu 4d, and Zr 3d in 5HEO-NCM811 are obvious, while they are inconspicuous in the NCM811 sample. This also shows the presence of HEO on the surface of HEO-NCM811.

The alkaline Li-based impurities (such as Li_2CO_3) formed by Reactions (1)–(4) between Ni-rich cathode and air are responsible for the difficulty in slurry processing [40,41]. Alkaline environments tend to induce the defluorination of poly(vinyl difluoride) (PVDF) binders, which then lead to particle agglomeration and a sudden increase in the slurry viscosity during cathode fabrication [34]. To explore the effect on the processing of this strategy, the rheological properties of slurries were tested. Except for the active material, the slurries of NCM811 and 5HEO-NCM811 have the same composition, ratio, and solid content. Firstly, for the laboratory commonly-used slurries with a weight ratio of cathode:PVDF:AB = 8:1:1 and a solid content of 29.4%, as shown in Fig. 4(a), the viscosity of the NCM811 slurry is higher than that of the 5HEO-NCM811 slurry across the entire test range, especially at the low shear rate. Strikingly, when the shear rate is 50 s^{-1}, HEO coating reduces the slurry viscosity from 4.9 Pa·s (NCM811) to 3.9 Pa·s (5HEO-NCM811) (Fig. 4(c)). In addition, the amplitude sweeps were used to compare the rheological properties of the two slurries in detail (Figs. 4(b) and 4(c)). In Fig. 4(b), the storage moduli (G') of the two pair curves dominate over the loss moduli (G'') under low shear range, but the opposite in high shear range. When G' is higher than G'', the slurry is solid-like and mainly elastically deformed; when G' is less than G'', the slurry is mainly viscous deformation and exhibits liquid-like characteristics [27]. The intersection point location is often used to

assess the stability of slurry and the potential for increasing the solid content. The results show that the intersection point of NCM811 is on the right side of 5HEO-NCM811, indicating that NCM811 slurry has better stability than that of 5HEO-NCM811 slurry at this solid content. That is, the HEO coating increases the potential for an enhanced solid content in the NCM811 slurry [4].

$$Ni^{3+} + O^{2-}_{lattice} \rightarrow Ni^{2+} + O^{-} \quad (1)$$

$$O^{-} + O^{-} \rightarrow O^{2-}_{active} + O \quad (2)$$

$$O^{2-}_{active} + CO_2/H_2O \rightarrow CO_3^{2-}/2OH^{-} \quad (3)$$

$$Li^{3+} + CO_3^{2-}/2OH^{-} \rightarrow Li_2CO_3/2LiOH \quad (4)$$

Subsequently, viscosity and rheology tests were also performed for slurries with a higher active substance content (cathode:PVDF:AB = 92:4:4 in weight) and the higher solid contents (61.5% and 65.3%) in order to get closer to the practical production, as shown in Figs. 4(d)–4(f). Both cathode materials showed an increase in the viscosity as the solid content increased. However, the 5HEO-NCM811 slurry possessed a

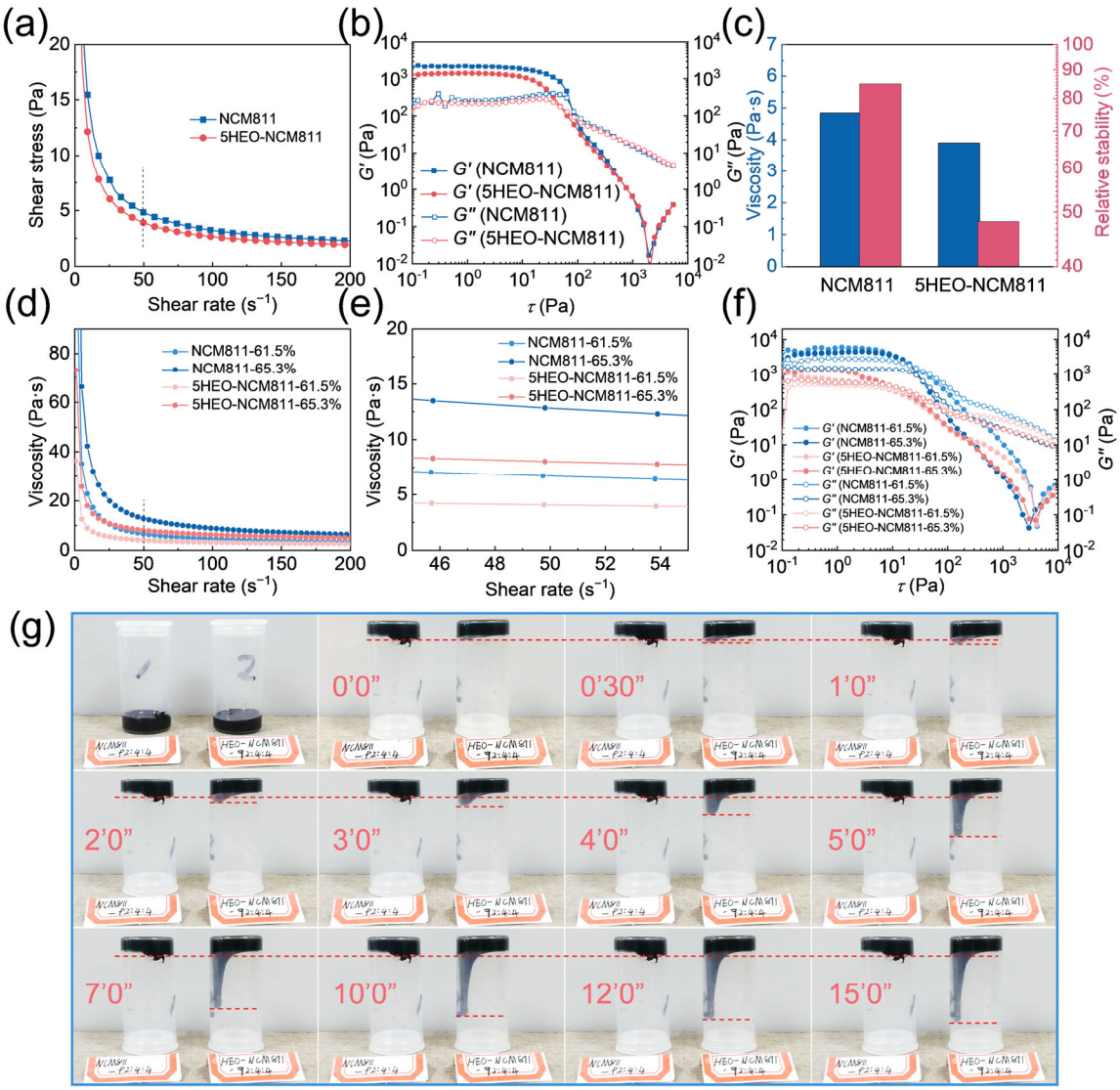

Fig. 4 (a) Viscosity curves and (b) amplitude sweeps of NCM811 and 5HEO-NCM811-based slurries with the weight ratio of 8:1:1 (cathode:PVDF:AB) and the solid content of 29.4%. (c) Comparison of the corresponding viscosities and relative stabilities of the two samples. (d, e) Viscosity curves and (f) amplitude sweeps of NCM811 and 5HEO-NCM811-based slurries with the weight ratio of 92:4:4 (cathode:PVDF:AB) and the solid contents of 61.5% and 65.3%. (g) Photographs of the NCM811 and 5HEO-NCM811-based slurries with the weight ratio of 92:4:4 (cathode:PVDF:AB) and the solid content of 65.3% and the flow processes of these two samples.

lower viscosity compared to the NCM811 slurry with the same solid content. That is, at a solid content of 61.5%, the viscosity of NCM811 is 6.7 Pa·s and that of 5HEO-NCM811 is 4.1 Pa·s. When the solid content rises to 65.3%, the viscosities of NCM811 and 5HEO-NCM811 are 12.8 and 8.0 Pa·s, respectively. As for the amplitude mode, as shown in Fig. 4(e), the intersection point of the 5HEO-NCM811 slurry is smaller than that of NCM811 at the same solid content. To more visually show the enhancement of the processing performance of NCM811 by HEO coating, the fluidity of these two kinds of slurries with the weight ratio of 92:4:4 (cathode: PVDF:AB) and the solid content of 65.3% were recorded as shown in Fig. 4(f). In the beginning, both slurries had the same liquid level (the amount of slurry was the same), and when inverted reagent bottle, the slurry of 5HEO-NCM811 flowed slowly downward for the first three minutes, and the distance increased rapidly within 3–7 min and basically flowed to the bottom by the 15th minute. In contrast, the slurry of NCM811 barely flowed throughout the process. It can be concluded that this strategy can increase the fluidity and solid content of NCM811 slurry, reducing the amount of solvent and lowering the production cost.

In order to evaluate the benefits of the electrochemical performance brought about by HEO coating, the assembled half-cells were charged/discharged with the voltage range of 2.8–4.3 V at 1 C. The electrochemical performances of NCM811 and *x*HEO-NCM811 (x = 1, 3, 5, and 10) cathodes were tested. As shown in Fig. 5(a), at the current density of 0.1 C, 1HEO-NCM811 delivers the highest capacity (194.7 $mA{\cdot}h{\cdot}g^{-1}$), while 10HEO-NCM811 is the lowest one (159.3 $mA{\cdot}h{\cdot}g^{-1}$). In addition, NCM811, 3HEO-NCM811, and 5HEO-NCM811 electrodes deliver 190.5, 187.6, and 185.8 $mA{\cdot}h{\cdot}g^{-1}$, respectively. Since the HEO is inactive in the voltage range of 2.8–4.3 V, the initial capacity decreases as the amount of coating increases. However, the reduction of the content in the range of 0–5 wt% is relatively small. When the coating amount is 10 wt%, the capacity decreases significantly, so it can be considered that this coating amount is excessive. In order to investigate the influence of each coating amount on the capacity attenuation, the cycling performance of each electrode was normalized. As shown in Fig. 5(b), after 300 cycles at 1 C, the capacity retention of NCM811, 1HEO-NCM811, 3HEO-NCM811, 5HEO-NCM811, and 10HEO-NCM811 electrodes are 57.3%, 67.6%, 68.1%, 74.2%, and 66.6%, respectively. Compared with NCM811, the capacity retention of the HEO coated NCM811 has improved to varying degrees. The cycle retention also increased upon the amount of coating increased from 0 to 5 wt%. The possible reason is that the HEO coating layer prevents NCM811 from contacting the electrolyte, reducing the side reactions between the electrode and the electrolyte. That is, the HEO coating layer reduces the cycle attenuation caused by the side reaction between the electrode and the electrolyte.

The CV test was carried out to further investigate the influence of HEO coating on the electrochemical parameters of NCM811. The first two-cycle CV curves of NCM811 (blue curves) and 5HEO-NCM811 (red curves) with a scan rate of 0.1 $mV{\cdot}s^{-1}$ in the voltage range of 2.8–4.3 V are shown in Fig. 5(c). Both samples show three typical pairs of redox peaks of Ni-rich cathode materials: hexagonal phase (H1)–monoclinic phase (M), M–new hexagonal phase (H2), and H2–hexagon phase (H3) [36]. The initial redox peaks in the first cycle of NCM811 are located at 3.81 V (H1–M) and 3.71 V (M–H1), and the potential difference is 0.104 V. The peak potential difference in the second cycle is 0.058 V. In contrast, the peak potential differences in the first cycle and the second cycle of 5HEO-NCM811 are 0.066 and 0.037 V, respectively, which are both smaller than those of NCM811. The results show that HEO coating layer can reduce the electrochemical polarization and improve the reversibility, playing a positive role in the rate performance and cycling stability. In addition, the potential difference between the oxidation peak position of the first cycle and the second cycle of 5HEO-NCM811 is smaller than that of NCM811. This also shows that HEO coating layer can reduce the irreversible capacity during the first charge. To verify the benefits inferred from the CV results, the rate performance of NCM811 and *x*HEO-NCM811 were tested at different current densities from 0.1 to 5 C between 2.8 and 4.3 V. There is little difference in the rate performance of these materials. As shown in Fig. 5(d), the capacity retention rates of NCM811, 1HEO-NCM811, 3HEO-NCM811, 5HEO-NCM811, and 10HEO-NCM811 at 5 C (the 55th cycle) are 71.38%, 73.19%, 74.12%, 74.69%, and 72.14%, respectively. Generally, oxide coating will reduce the rate performance by hindering the ion migration [7]. However, the HEO coating did not decrease but slightly improved the rate performance. Therefore, the Li-ion diffusion coefficients (D_{Li^+}) of NCM811 and 5HEO-NCM811 were evaluated. The CV curves of NCM811 and 5HEO-NCM811 at

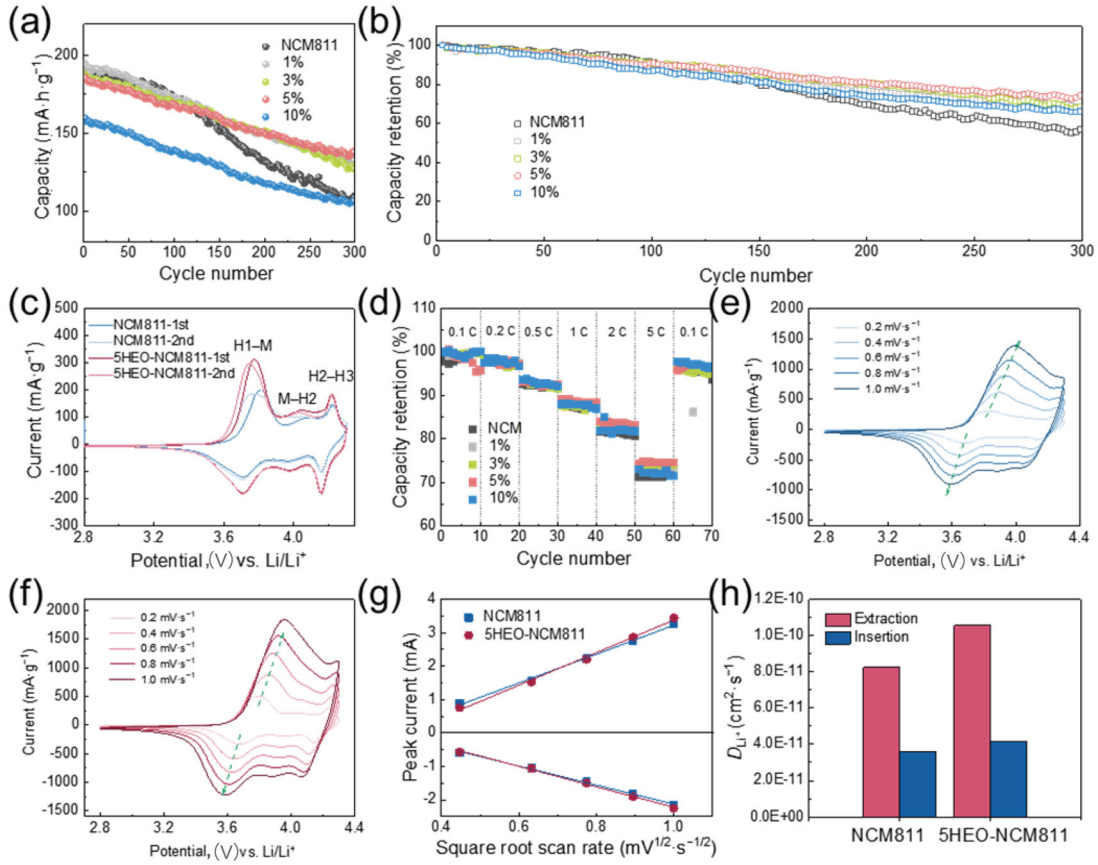

Fig. 5 (a) Cycling performances and (b) normalized cycling performances of NCM811, 1HEO-NCM811, 3HEO-NCM811, 5HEO-NCM811, and 10HEO-NCM811. (c) CV curves of NCM811 and 5HEO-NCM811. (d) Normalized rate performances. CV curves of (e) NCM811 and (f) 5HEO-NCM811 at various scan rates. (g) Relationship of peak current and square root scan rate. (h) D_{Li^+} of NCM811 and 5HEO-NCM811.

various scan rates of 0.2, 0.4, 0.6, 0.8, and 1 mV·s^{-1} are shown in Figs. 5(e) and 5(f), respectively. The relationship between the peak current and square root scan rate is illustrated in Fig. 5(g). Finally, the D_{Li^+} is calculated by the Randles–Sevcik equation:

$$i_p = 2.69\times10^5 n^{3/2} A C_0 D_{Li^+}^{1/2} v^{1/2} \quad (5)$$

where i_p, n, A, C_0, and v represent the peak current, the number of electrons in redox reaction, the area of electrode, the molarity of lithium ions, and the scan rate, respectively. As shown in Fig. 5(h), D_{Li^+} of the two samples have the same order of magnitude, indicating that the HEO coating layer does not hinder the diffusion of Li^+. However, compared to NCM811, the D_{Li^+} of 5HEO-NCM811 is slightly larger. This is because the amount of HEO coating is very small relative to that of the bulk material, and the coating layer suppresses the side reaction at the electrode–electrolyte interface, and thus the Li-ion diffusion is slightly improved.

To further explore the reasons for better electrochemical performances of the coated samples, the EIS, SEM, and XPS were employed to study the morphology and the surface CEI component of the cycled material. The EIS was performed with a frequency range of 10^{-2}–10^5 Hz after 300 cycles. As shown in Fig. S3 in the ESM, compared with Li||5HEO-NCM811, Li||NCM811 half-cell shows a greater impedance, resulting from the resistance of the thick CEI on the surface. The morphologies of NCM811 and 5HEO-NCM811 after 300 cycles are shown in Figs. 6(a) and 6(b), respectively. The secondary particles of NCM811 are obviously broken, and there is a thick layer of sediment on the surface which makes the morphology of the primary particles become blurred. In contrast, the particles of the cycled 5HEO-NCM811 remained intact. The surface morphology did not change much compared with that before the cycle, no obvious deposits were observed, and the primary particles were clearly visible. For F 1s in the cycled NCM811 (Fig. 6(c)) and 5HEO-NCM811 (Fig. 6(d)), the peaks at

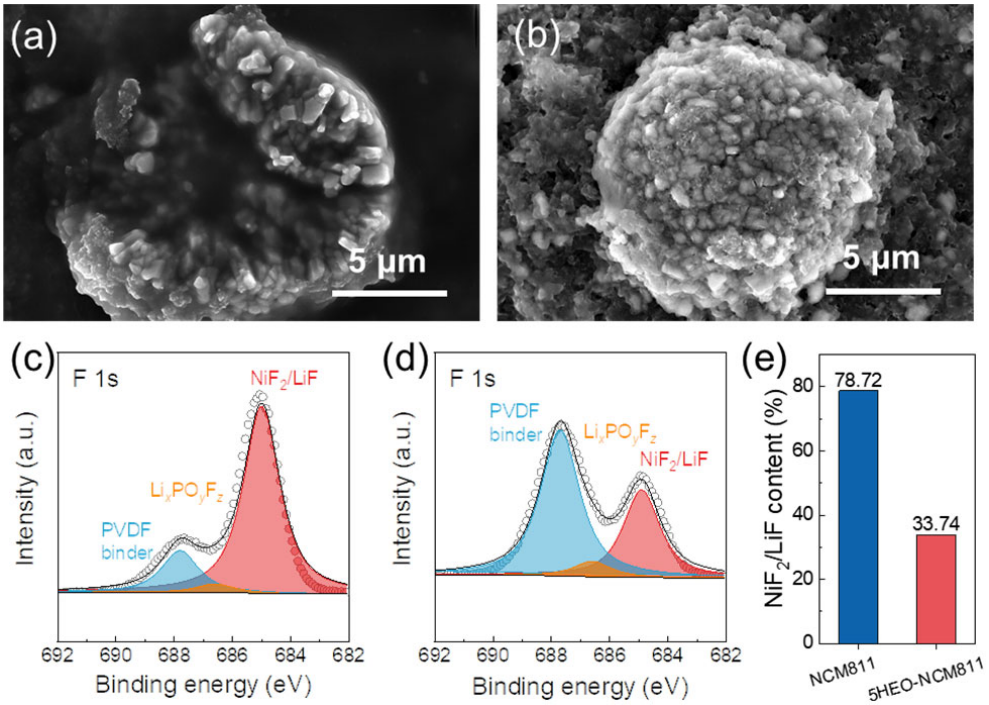

Fig. 6 SEM images of (a) NCM811 and 5HEO-NCM811 electrodes after 300 cycles at 1 C. F 1s XPS spectra of (c) NCM811 and (d) 5HEO-NCM811 after 300 cycles at 1 C, and (e) corresponding NiF_2/LiF contents of these two samples.

687.8, 686.6, and 685.0 eV are attributed to PVDF, $Li_xPO_yF_z$, and NiF_2/LiF, respectively. $Li_xPO_yF_z$ and NiF_2/LiF are considered as the electrolyte decomposition product and component of CEI, respectively [42]. As shown in Fig. 6(e), the content of NiF_2/LiF in the cycled NCM811 is 78.72%, which is more than twice that in the cycled 5HEO-NCM811 (33.74%). This fully proves that the HEO coating layer improves the cycle stability by reducing the interface side reactions and reducing polarization.

4 Conclusions

In summary, the HEO coated NCM811 cathode material was successfully prepared for the first time using a facile self-ball milling method. The results of a series of physical and chemical tests (such as the XPS and SEM) show that the HEO nanosheets are distributed on the surface in a discontinuous form. The HEO coating effectively reduces the contact of NCM811 with air and electrolyte, hinders the formation of Li_2CO_3/LiOH, inhibits the side reaction of NCM811 and residual lithium compound with electrolyte, and protects the cathode material from HF corrosion. These positive effects of HEO coating, especially when the coating amount is 5 wt%, significantly reduce the polarization of the battery, and increase the capacity retention rate from 57.3% (NCM811) to 74.2% (5HEO-NCM811) after 300 cycles at 1 C. Meanwhile, the coating will not negatively affect the Li-ion diffusion and rate performance. The SEM and XPS test results of the cycled electrodes further prove that the HEO coated NCM811 can prolong the charge–discharge cycle by suppressing side reactions at the electrode–electrolyte interface. In addition, the slurry of 5HEO-NCM811 has a lower viscosity at the same solid content, and the processing performance is substantially improved. This strategy provides a new reasonable path to the coating modification of the Ni-rich cathode material, providing a new idea for high-performance LIB cathode materials.

Acknowledgements

The authors acknowledge the financial support provided by the Science, Technology, and Innovation Commission of Shenzhen Municipality (JCYJ20180508151856806), the Key R&D Program of Shaanxi (2019ZDLGY04-05), the National Natural Science Foundation of Shaanxi Province (2019JLZ-01), and the Fundamental Research Funds for the Central Universities (19GH020302, 3102019JC005, 3102021ZD0401, and 3102021TS0406).

Electronic Supplementary Material

Supplementary material is available in the online version of this article at https://doi.org/10.1007/s40145-022-0582-6.

References

[1] Cano ZP, Banham D, Ye S, *et al*. Batteries and fuel cells for emerging electric vehicle markets. *Nat Energy* 2018, **3**: 279–289.

[2] Kwade A, Haselrieder W, Leithoff R, *et al*. Current status and challenges for automotive battery production technologies. *Nat Energy* 2018, **3**: 290–300.

[3] Yoon MS, Dong YH, Hwang JS, *et al*. Reactive boride infusion stabilizes Ni-rich cathodes for lithium-ion batteries. *Nat Energy* 2021, **6**: 362–371.

[4] Ning RQ, Yuan K, Zhang K, *et al*. A scalable snowballing strategy to construct uniform rGO-wrapped $LiNi_{0.8}Co_{0.1}Mn_{0.1}O_2$ with enhanced processability and electrochemical performance. *Appl Surf Sci* 2021, **542**: 148663.

[5] Zhou JW, Han ZX, Zhang YY, *et al*. Design and host-involved *in situ* fabrication of La_4NiLiO_8 coating on Ni-rich cathode materials towards superior structural stability. *J Mater Chem A* 2021, **9**: 3427–3440.

[6] Cherkashinin G, Motzko M, Schulz N, *et al*. Electron spectroscopy study of Li[Ni,Co,Mn]O_2/electrolyte interface: Electronic structure, interface composition, and device implications. *Chem Mater* 2015, **27**: 2875–2887.

[7] Tan XR, Zhang ML, Li J, *et al*. Recent progress in coatings and methods of Ni-rich $LiNi_{0.8}Co_{0.1}Mn_{0.1}O_2$ cathode materials: A short review. *Ceram Int* 2020, **46**: 21888–21901.

[8] Liu W, Li XF, Hao YC, *et al*. Functional passivation interface of $LiNi_{0.8}Co_{0.1}Mn_{0.1}O_2$ toward superior lithium storage. *Adv Funct Mater* 2021, **31**: 2008301.

[9] Park CW, Lee J-H, Seo JK, *et al*. Graphene collage on Ni-rich layered oxide cathodes for advanced lithium-ion batteries. *Nat Commun* 2021, **12**: 2145.

[10] Strauss F, Teo JH, Maibach J, *et al*. Li_2ZrO_3-coated NCM622 for application in inorganic solid-state batteries: Role of surface carbonates in the cycling performance. *ACS Appl Mater Interfaces* 2020, **12**: 57146–57154.

[11] Wang WZ, Wu LY, Li ZW, *et al*. *In situ* tuning residual lithium compounds and constructing TiO_2 coating for surface modification of a nickel-rich cathode toward high-energy lithium-ion batteries. *ACS Appl Energy Mater* 2020, **3**: 12423–12432.

[12] Hofmann M, Nagler F, Guntow U, *et al*. Long-term cycling performance of aqueous processed Ni-rich $LiNi_{0.8}Co_{0.15}Al_{0.05}O_2$ cathodes. *J Electrochem Soc* 2021, **168**: 060511.

[13] Qiu L, Xiang W, Tian W, *et al*. Polyanion and cation co-doping stabilized Ni-rich Ni–Co–Al material as cathode with enhanced electrochemical performance for Li-ion battery. *Nano Energy* 2019, **63**: 103818.

[14] Yeh J-W, Chen S-K, Lin S-J, *et al*. Nanostructured high-entropy alloys with multiple principal elements: Novel alloy design concepts and outcomes. *Adv Eng Mater* 2004, **6**: 299–303.

[15] Oses C, Toher C, Curtarolo S. High-entropy ceramics. *Nat Rev Mater* 2020, **5**: 295–309.

[16] Lökçü E, Toparli Ç, Anik M. Electrochemical performance of $(MgCoNiZn)_{1-x}Li_xO$ high-entropy oxides in lithium-ion batteries. *ACS Appl Mater Interfaces* 2020, **12**: 23860–23866.

[17] Zhang R-Z, Reece MJ. Review of high entropy ceramics: Design, synthesis, structure and properties. *J Mater Chem A* 2019, **7**: 22148–22162.

[18] Sarkar A, Velasco L, Wang D, *et al*. High entropy oxides for reversible energy storage. *Nat Commun* 2018, **9**: 3400.

[19] Li F, Zhou L, Liu J-X, *et al*. High-entropy pyrochlores with low thermal conductivity for thermal barrier coating materials. *J Adv Ceram* 2019, **8**: 576–582.

[20] Xiang HM, Xing Y, Dai F-Z, *et al*. High-entropy ceramics: Present status, challenges, and a look forward. *J Adv Ceram* 2021, **10**: 385–441.

[21] Lun Z, Ouyang B, Kwon D-H, *et al*. Cation-disordered rocksalt-type high-entropy cathodes for Li-ion batteries. *Nat Mater* 2021, **20**: 214–221.

[22] Wang QS, Sarkar A, Wang D, *et al*. Multi-anionic and -cationic compounds: New high entropy materials for advanced Li-ion batteries. *Energy Environ Sci* 2019, **12**: 2433–2442.

[23] Nguyen TX, Patra J, Chang J-K, *et al*. High entropy spinel oxide nanoparticles for superior lithiation–delithiation performance. *J Mater Chem A* 2020, **8**: 18963–18973.

[24] Zhao CL, Ding FX, Lu YX, *et al*. High-entropy layered oxide cathodes for sodium-ion batteries. *Angew Chem Int Ed* 2020, **59**: 264–269.

[25] Rost CM, Sachet E, Borman T, *et al*. Entropy-stabilized oxides. *Nat Commun* 2015, **6**: 8485.

[26] Tu T-Z, Liu J-X, Zhou L, *et al*. Graceful behavior during CMAS corrosion of a high-entropy rare-earth zirconate for thermal barrier coating material. *J Eur Ceram Soc* 2022, **42**: 649–657.

[27] Bauer W, Nötzel D. Rheological properties and stability of NMP based cathode slurries for lithium ion batteries. *Ceram Int* 2014, **40**: 4591–4598.

[28] Teng Z, Zhu LN, Tan YQ, *et al*. Synthesis and structures of high-entropy pyrochlore oxides. *J Eur Ceram Soc* 2020, **40**: 1639–1643.

[29] Mao H-R, Guo R-F, Cao Y, *et al*. Ultrafast densification of high-entropy oxide $(La_{0.2}Nd_{0.2}Sm_{0.2}Eu_{0.2}Gd_{0.2})_2Zr_2O_7$ by reactive flash sintering. *J Eur Ceram Soc* 2021, **41**: 2855–2860.

[30] You LZ, Chu BB, Li GX, *et al*. H_3BO_3 washed $LiNi_{0.8}Co_{0.1}Mn_{0.1}O_2$ with enhanced electrochemical performance and storage characteristics. *J Power Sources* 2021, **482**: 228940.

[31] Yang HP, Wu H-H, Ge MY, *et al*. Simultaneously dual

modification of Ni-rich layered oxide cathode for high-energy lithium-ion batteries. *Adv Funct Mater* 2019, **29**: 1808825.

[32] Xu CL, Xiang W, Wu ZG, *et al*. Dual-site lattice modification regulated cationic ordering for Ni-rich cathode towards boosted structural integrity and cycle stability. *Chem Eng J* 2021, **403**: 126314.

[33] Kim Y, Park H, Warner JH, *et al*. Unraveling the intricacies of residual lithium in high-Ni cathodes for lithium-ion batteries. *ACS Energy Lett* 2021, **6**: 941–948.

[34] You Y, Celio H, Li JY, *et al*. Modified high-nickel cathodes with stable surface chemistry against ambient air for lithium-ion batteries. *Angew Chem Int Ed* 2018, **57**: 6480–6485.

[35] Quinlan RA, Lu Y-C, Kwabi DG, *et al*. XPS investigation of the electrolyte induced stabilization of $LiCoO_2$ and "$AlPO_4$"-coated $LiCoO_2$ composite electrodes. *J Electrochem Soc* 2015, **163**: A300–A308.

[36] Yuan K, Li N, Ning RQ, *et al*. Stabilizing surface chemical and structural Ni-rich cathode via a non-destructive surface reinforcement strategy. *Nano Energy* 2020, **78**: 105239.

[37] Kim U-H, Park N-Y, Park G-T, *et al*. High-energy W-doped $Li[Ni_{0.95}Co_{0.04}Al_{0.01}]O_2$ cathodes for next-generation electric vehicles. *Energy Storage Mater* 2020, **33**: 399–407.

[38] Wu LP, Tang XC, Rong ZH, *et al*. Studies on electrochemical reversibility of lithium tungstate coated Ni-rich $LiNi_{0.8}Co_{0.1}Mn_{0.1}O_2$ cathode material under high cut-off voltage cycling. *Appl Surf Sci* 2019, **484**: 21–32.

[39] White JL, Gittleson FS, Homer M, *et al*. Nickel and cobalt oxidation state evolution at Ni-rich NMC cathode surfaces during treatment. *J Phys Chem C* 2020, **124**: 16508–16514.

[40] Su YF, Li LW, Chen G, *et al*. Strategies of removing residual lithium compounds on the surface of Ni-rich cathode materials. *Chin J Chem* 2021, **39**: 189–198.

[41] Kim J, Lee H, Cha H, *et al*. Prospect and reality of Ni-rich cathode for commercialization. *Adv Energy Mater* 2018, **8**: 1702028.

[42] Li W, Dolocan A, Oh P, *et al*. Dynamic behaviour of interphases and its implication on high-energy-density cathode materials in lithium-ion batteries. *Nat Commun* 2017, **8**: 14589.